

# Geophysical Research Letters<sup>®</sup>



## RESEARCH LETTER

10.1029/2023GL104807

### Key Points:

- Surface temperature gradients and vorticity anomalies at scales down to  $O(10)$  km impact wind stress curl and divergence jointly
- Wind-front interactions at sub-mesoscales are at least an order of magnitude stronger than at mesoscales
- Reconstruction of the wind stress curl using both thermal and current feedback is 10%–40% more accurate than relying on a single feedback

### Supporting Information:

Supporting Information may be found in the online version of this article.

### Correspondence to:

Y. Bai,  
ybbai@caltech.edu

### Citation:

Bai, Y., Thompson, A. F., Villas Bôas, A. B., Klein, P., Torres, H. S., & Menemenlis, D. (2023). Sub-mesoscale wind-front interactions: The combined impact of thermal and current feedback. *Geophysical Research Letters*, *50*, e2023GL104807. <https://doi.org/10.1029/2023GL104807>

Received 6 JUN 2023  
Accepted 2 SEP 2023

## Sub-Mesoscale Wind-Front Interactions: The Combined Impact of Thermal and Current Feedback

Yue Bai<sup>1</sup> , Andrew F. Thompson<sup>1</sup> , Ana B. Villas Bôas<sup>2</sup> , Patrice Klein<sup>1,3</sup> , Hector S. Torres<sup>3</sup> , and Dimitris Menemenlis<sup>3</sup> 

<sup>1</sup>California Institute of Technology, Pasadena, CA, USA, <sup>2</sup>Colorado School of Mines, Golden, CO, USA, <sup>3</sup>Jet Propulsion Laboratory, La Cañada Flintridge, CA, USA

**Abstract** Surface ocean temperature and velocity anomalies at meso- and sub-meso-scales induce wind stress anomalies. These wind-front interactions, referred to as thermal (TFB) and current (CFB) feedbacks, respectively, have been studied in isolation at mesoscale, yet they have rarely been considered in tandem. Here, we assess the combined influence of TFB and CFB and their relative impact on surface wind stress derivatives. Analyses are based on output from two regions of the Southern Ocean in a coupled simulation with local ocean resolution of 2 km. Considering both TFB and CFB shows regimes of interference, which remain mostly linear down to the simulation resolution. The jointly-generated wind stress curl anomalies approach  $10^{-5}$  N m<sup>-3</sup>,  $\sim 20$  times stronger than at mesoscale. The synergy of both feedbacks improves the ability to reconstruct wind stress curl magnitude and structure from both surface vorticity and SST gradients by 12%–37% on average, compared with using either feedback alone.

**Plain Language Summary** Surface ocean temperature and velocity anomalies at 0.1–100 km scales imprint their signatures on the surface wind stress, which in turn supplies the ocean with momentum. This process is called wind-front interaction and typically referred to as thermal and current feedbacks when generated by temperature gradients and velocity gradients, respectively. Previously, studies using satellite observations and regional numerical models have studied either feedback in isolation; consideration of both feedbacks in tandem remains immature. Here, we present an approach that assesses both feedbacks' combined and relative impact on the surface wind stress, using output from an air-sea coupled simulation. This approach allows us to identify constructive and destructive patterns of how the two feedbacks interact, which remain mostly linear down to the simulation resolution. The jointly-generated wind stress derivative anomalies are 20 times stronger than observed previously at larger scales. Considering both feedbacks, reconstructions of wind stress derivatives are viable and have 10%–40% less error on average compared with using either feedback by itself. Contributions from either feedback in modifying wind stress fields vary temporally and can be related to physical properties such as surface wind speed and air-sea temperature difference across the studied area.

## 1. Introduction

The exchange of heat and momentum between the ocean and the atmosphere is a critical component of global climate evolution. Processes that govern air-sea coupling and the transfer of climate-relevant tracers occur across a broad range of scales (Chang et al., 2020; Renault et al., 2018; Seo et al., 2023; Small et al., 2019; Strobach et al., 2022), with transitions in air-sea behavior occurring at a few key spatial scales. At the basin scale, the atmosphere supplies the momentum that powers the ocean currents (Rai et al., 2021) and determines the oceanic distribution of latent and sensible heat fluxes (Small et al., 2008, 2019). At oceanic mesoscale, or spatial scales of  $O(100)$  km and Rossby number  $Ro = \zeta/f \ll 1$  (where  $\zeta$  is the vertical component of relative vorticity), these relationships reverse and ocean surface variability triggers atmospheric responses (Chelton & Xie, 2010; Frenger et al., 2013; Renault et al., 2016; Seo et al., 2023; Small et al., 2019). This change in behavior occurs due to two dynamical processes that become relevant at the scale of ocean mesoscale eddies: the thermal and current feedbacks (TFB and CFB), which are related to surface ocean temperature gradients and velocity gradients, respectively. Wind-front interactions have been studied almost exclusively using satellite products (e.g., Chelton et al., 2004) and mesoscale-resolving numerical simulations (e.g., Renault et al., 2016; Takatama & Schneider, 2017). In the ocean, however, another dynamical transition occurs at  $O(10)$  km, scales smaller than the mesoscale, where the Rossby number approaches  $O(1)$ . Hereafter, we refer to  $O(10)$  km and  $Ro \gtrsim 1$  motions as “sub-mesoscale.” While the impact of these sub-mesoscale features on air-sea interactions remains

© 2023. The Authors.

This is an open access article under the terms of the [Creative Commons Attribution-NonCommercial-NoDerivs License](https://creativecommons.org/licenses/by-nc-nd/4.0/), which permits use and distribution in any medium, provided the original work is properly cited, the use is non-commercial and no modifications or adaptations are made.

largely unconstrained, they are characterized by strong anomalies in vorticity and density gradients (Balwada et al., 2018; Siegelman et al., 2020; Taylor & Thompson, 2023) that may contribute to the TFB and CFB.

The thermal component of wind-front interactions assesses the “bottom-up” (Renault et al., 2018) thermodynamic influence of sea surface temperature (SST) gradients on the atmospheric wind fields (Chelton et al., 2004). Fore-runner studies, such as Chelton et al. (2001); Chelton et al. (2004); O’Neill et al. (2012), empirically established positive linear relationships between wind stress divergence and wind stress curl with downwind and crosswind SST gradients (defined in Section 3.1), respectively. Mechanisms that support the TFB coupling were reviewed in detail by Small et al. (2008). Gradients in SST modify the overlying atmospheric boundary layer stability and the surface drag coefficient. This in turn generates mesoscale variability in wind speed and stress through either pressure adjustment or downward momentum transfer (Desbiolles et al., 2023; Frenger et al., 2013). Chelton et al. (2007); Chelton et al. (2011); O’Neill et al. (2012) quantified these correlations through linear coupling coefficients and found seasonal fluctuations in the coupling intensity (Chelton & Xie, 2010). The TFB influences the distribution of latent and sensible heat fluxes (Foussard et al., 2019), and induces wind stress curl anomalies that can enhance Ekman pumping, especially in the Southern Ocean (Gaubé et al., 2015).

Current feedback (CFB), the mechanical driver of wind-front interactions, arises from the difference between surface vector winds and surface ocean currents. Since mesoscale eddies are typically of smaller spatial scale than atmospheric variations, the air-sea velocity difference is non-uniform across the eddy. This feature causes eddies with positive vorticity to generate a negative wind stress curl anomaly (Renault et al., 2016), and eddies with negative vorticity to generate a positive wind stress curl anomaly (Rai et al., 2021). Bye (1985); Rooth and Xie (1992) showed analytically that the negative correlation between vorticity and wind stress curl is linearly dependent on the magnitude of the local surface wind speed. Renault et al. (2017) used mesoscale satellite observations to confirm that the current-stress coupling coefficient depends on local surface wind speed. CFB is a sink of the oceanic mesoscale geostrophic kinetic energy to the atmosphere (Renault et al., 2016; Xu & Scott, 2008). This “eddy killing” effect acts through the wind stress curl-induced Ekman pumping (Gaubé et al., 2015) that counteracts the eddy vorticity and therefore weakens the eddies (Renault et al., 2018). At mesoscales, where flows are to leading order geostrophic and divergence-free, the connection between surface current divergence and wind stress divergence is often neglected (Renault et al., 2018).

Recent high-resolution numerical simulations have enabled a first exploration of sub-mesoscale wind-front feedbacks, which are shown to be significantly enhanced compared with those at mesoscales. Strobach et al. (2022) focused on SST fronts of  $\sim 10$  km in the Gulf Stream using a sub-mesoscale-resolving coupled simulation. These SST gradients are up to 20 times stronger than those observed in pioneering mesoscale studies (e.g., Chelton et al., 2004), and they generate large wind stress curl anomalies up to  $10^{-5}$  N m $^{-3}$ . In an idealized simulation, Chen et al. (2022) confirmed the enhancement of CFB due to sub-mesoscale surface vorticity anomalies that exceed the local Coriolis parameter  $f$ . At the sub-mesoscale, flow begins to escape the constraint of Earth’s rotation, and surface divergence starts to assume a comparable magnitude as the surface vorticity (Callies et al., 2020; McWilliams, 2016; Thomas et al., 2008). At those small spatial scales, a negative linear correlation between surface divergence and wind stress divergence was recently identified (Chen et al., 2022), in addition to the well-established correlation between ocean vorticity and wind stress curl. The impact of sub-mesoscale wind-front interactions on globally-integrated heat and momentum budgets are yet to be quantified.

Most previous studies, including recent studies that resolve sub-mesoscales, quantify wind stress derivatives as a function of either TFB or CFB, but rarely consider the two processes in tandem. Chelton et al. (2004) pointed out that strong density fronts are often collocated with strong currents and speculated that wind stress curl modifications from TFB could potentially be contaminated with CFB (Small et al., 2008). Renault et al. (2019) and Takatama and Schneider (2017) developed controlled mesoscale simulations to separate the two feedback mechanisms by only having one active at a given time, and identified their individual contribution to wind stress curl. However, in a coupled simulation or using observations, it is not possible to separate the impact on the wind stress derivatives from individual feedback mechanisms, and predictions from these “1D” studies, hereby referred to as 1D current or 1D thermal analysis, may be inaccurate due to the combination or cancellation of correlated TFB and CFB. In this study, we use output from a high-resolution coupled climate model to show that there is a large region of parameter space where an accurate prediction of wind stress derivatives requires accounting for both feedbacks. We adopt a “2D” perspective that incorporates both TFB and CFB and assesses their joint influence and relative importance simultaneously.

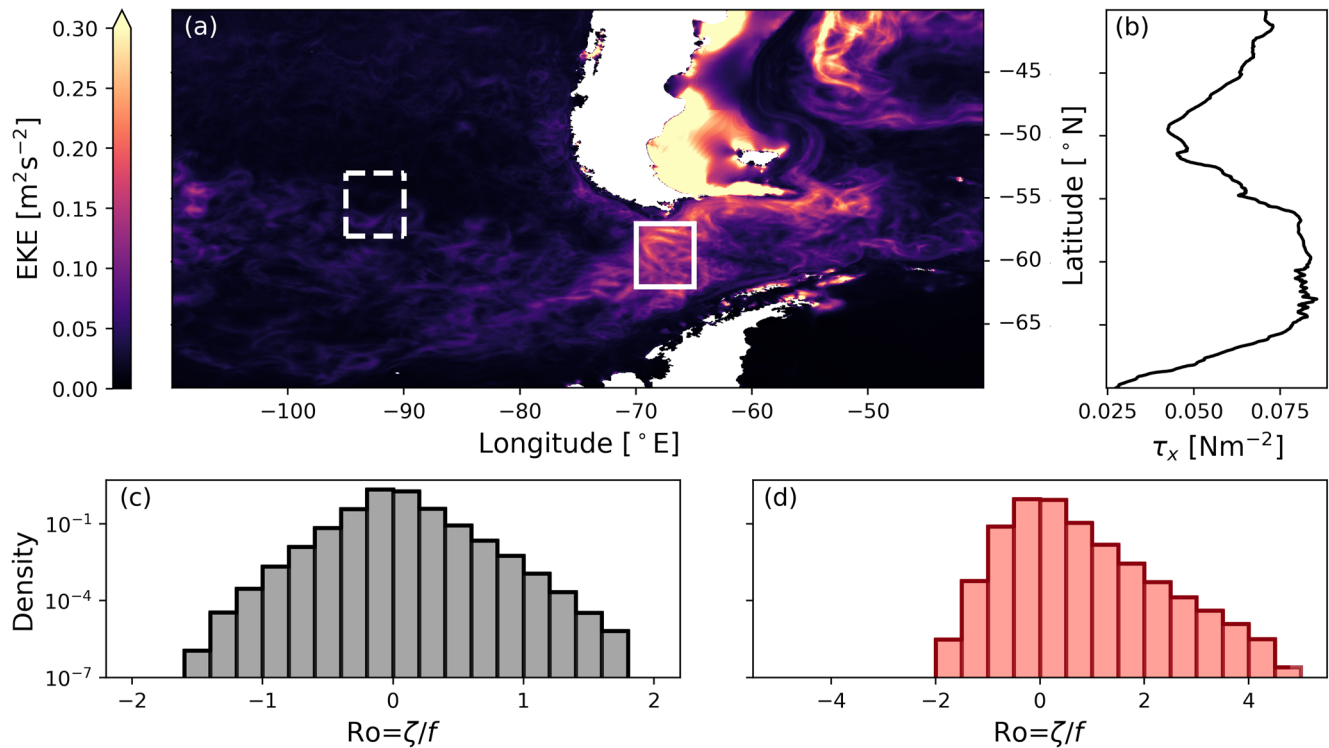


**Figure 1.** Southern Ocean study domains. (a) Mean surface eddy kinetic energy (EKE [ $\text{m}^2 \text{s}^{-2}$ ]) for austral winter months in 2012, taken from the COAS simulation (see Section 2), for the eastern Pacific sector of the Southern Ocean. The white boxes show two subdomains that are the focus of this study. The western (dashed) and eastern (solid) boxes correspond to quiescent ( $58\text{--}53^\circ\text{S}$ ,  $95\text{--}90^\circ\text{E}$ ) and energetic ( $62\text{--}57^\circ\text{S}$ ,  $70\text{--}65^\circ\text{E}$ ) regions, respectively. (b) Zonally-integrated zonal wind stress [ $\text{N m}^{-2}$ ] for the region shown in panel (a). (c) Histogram of Rossby number in the quiescent region; (d) Histogram of Rossby number in the energetic region.

## 2. Methods and Study Region

In this study, we use outputs from the state-of-the-art global Coupled Ocean-Atmosphere Simulation (COAS), commonly referred to as C1440-LLC2160. The oceanic component of COAS has a horizontal grid spacing of  $1/24^\circ$ , approximately 2 km around Antarctica. The atmospheric models has a nominal horizontal grid spacing of 6.9 km. The simulation was initialized on 20 January 2012, and results shown below are based on output from June 1st to 31 August 2012 (JJA). This configuration is identical to that used in Torres et al. (2022), from which the readers can find more general information on the model and experiment setup. The unprecedented spatial and temporal resolutions of this global coupled simulation make it a unique and necessary tool to study meso-to-sub-mesoscale wind-front interactions, a regime that remains under-explored.

The present study focuses on two subdomains that are within or close to the Drake Passage region of the Southern Ocean (Figure 1), where the impact of variable ocean surface properties is disproportionately large (Nicholson et al., 2022). We select this region because it is aligned with the westerly wind stress maximum (Figure 1b), and the Southern Ocean is a key site of air-sea exchange and ventilation (Dove et al., 2021; Gruber et al., 2019; Marshall & Speer, 2012), both of which may be impacted by vertical velocities linked to small-scale wind-front interactions (Gaube et al., 2015; Renault et al., 2023). Furthermore, the two  $5^\circ \times 5^\circ$  subdomains compare a quiescent, low eddy kinetic energy (EKE) regime, and a turbulent frontal region with higher background energy levels, the latter of which have been shown to localize and enhance ventilation (Dove et al., 2022, 2023). The surface Ro distribution (Figures 1c and 1d) for quiescent and energetic regions both favor cyclonic eddies and respectively have skewness values of 0.4 and 0.9, suggesting more sub-mesoscale fronts (Barkan et al., 2019; Buckingham et al., 2016) and frontal slumping (Hoskins & Bretherton, 1972) in the energetic region; Ro also has a larger magnitude in the energetic region.

In the following sections, we describe the 2D approach and the synergy of thermal and current feedbacks with output from the energetic region. These results do not depend on the dynamical processes that generate the SST gradients and vorticity anomalies; therefore we primarily focus on the statistical impact on wind-stress

gradients in this simulation. Results from the quiescent subdomain provided in Supplementary Information S1 offer preliminary insight into regional variations. A more thorough regional and temporal analysis of wind-front interactions is beyond the scope of this work.

### 3. Results

In this section, we consider the relative importance of both TFB and CFB by constructing a series of two-dimensional, binned-averaged, conditional mean plots that evaluate the joint dependence of wind stress curl and divergence on surface ocean vorticity/divergence and temperature gradients. We also quantify the relative contribution of each feedback on wind stress properties via linear coefficients, and investigate the temporal variability of these coefficients as well as the mechanisms that give rise to the variability.

#### 3.1. Combined Impact of Thermal and Current Feedbacks

The dependence of wind stress curl and divergence on surface ocean properties illustrates scenarios and regimes where, if considered using the 2D approach, CFB and TFB combine constructively and destructively. These regimes are evaluated by bin-averaging the hourly wind stress curl or divergence as a function of two properties, one chosen from each category: ocean vorticity and divergence, or crosswind and downwind SST gradient. Crosswind SST gradients are defined by  $\nabla SST \times \tau$  in which the winds are aligned with the front. For downwind SST gradients,  $\nabla SST \cdot \tau$ , the winds are perpendicular to the frontal direction. Ocean vorticity and divergence are normalized by the absolute value of  $f$ , while SST gradients are scaled by a typical sub-mesoscale frontal length scale,  $\sim 10$  km. Note that the normalizations are different from previous mesoscale studies in order to highlight sub-mesoscale features. A series of conditional mean plots (Figure 2) are constructed with non-uniform bin sizes as data points are sparse for extreme values; non-dimensionalized vorticity ( $\zeta/|f|$ ) and divergence ( $\delta/|f|$ ) have bin sizes ranging from 0.1 near 0 to 0.5 at  $\pm 4$ ; crosswind and downwind SST gradient bin sizes range from  $0.1^\circ\text{C}/10$  km near 0 to  $0.4^\circ\text{C}/10$  km at  $\pm 8$  (see further details in SI). These results are qualitatively similar when using uniform bin sizes. We calculate the mean and other statistical moments, using hourly output, to which we apply a one-day running mean to each field to remove high-frequency variability, likely related to atmospheric fluctuations. All values of wind stress curl/divergence over the full austral winter period (JJA, 2012) are collected for a given combination of vorticity/divergence and crosswind/downwind SST gradient, from which the standard deviation is calculated. Data that exceed  $\pm 1$  standard deviation, in each bin, are removed before computing the mean wind stress product to further minimize outliers introduced by synoptic events. The mean percentage of data removed in each panel ranges from 24.8% to 30.9%. The calculations of slopes and coefficients in Section 3.2 are not sensitive to this standard deviation cutoff.

There are eight possible combinations from two sets of surface variables as axes (ocean vorticity/divergence and cross/down-wind SST gradients): four for wind stress curl and four for wind stress divergence. Four are highlighted in Figure 2 that are representative of different CFB and TFB regimes. When only one property is relevant to the wind stress derivative, the conditional mean plot provides similar information as the independent 1D approach; when both properties are correlated with the wind stress field, the 2D perspective show patterns of interaction.

Between the two chosen axes of the conditional mean plot, if only one of the properties is contributing actively to wind-ocean feedbacks, then the wind stress derivative varies along a single axis, for example, Figures 2b and 2c. This essentially reduces to an independent 1D analysis. In Figure 2b, the mean wind stress divergence is close to zero when the downwind SST gradient is weak, for all values of surface vorticity. Positive downwind SST gradients lead to a positive wind stress divergence. This indicates that SST gradients and the TFB dominate small-scale structures in wind stress divergence, while surface vorticity plays a negligible role in setting small-scale variability. By averaging across surface vorticity values, the traditional 1D binned analysis of the TFB slope compares well with previous studies (e.g., Chelton & Xie, 2010). TFB also occurs where crosswind SST gradient is positively correlated with wind stress curl, while ocean divergence, as the other axis, has a limited impact (Figure 2c).

The conditional mean analysis also illustrates regimes where components from both CFB and TFB contribute to wind stress gradients. In Figure 2a, both vorticity and crosswind SST gradients shape small-scale variations in wind stress curl. For a given surface vorticity, wind stress curl increases linearly with crosswind SST gradient. However, meso- and smaller-scale features in wind stress curl are at the same time imprinted from surface ocean

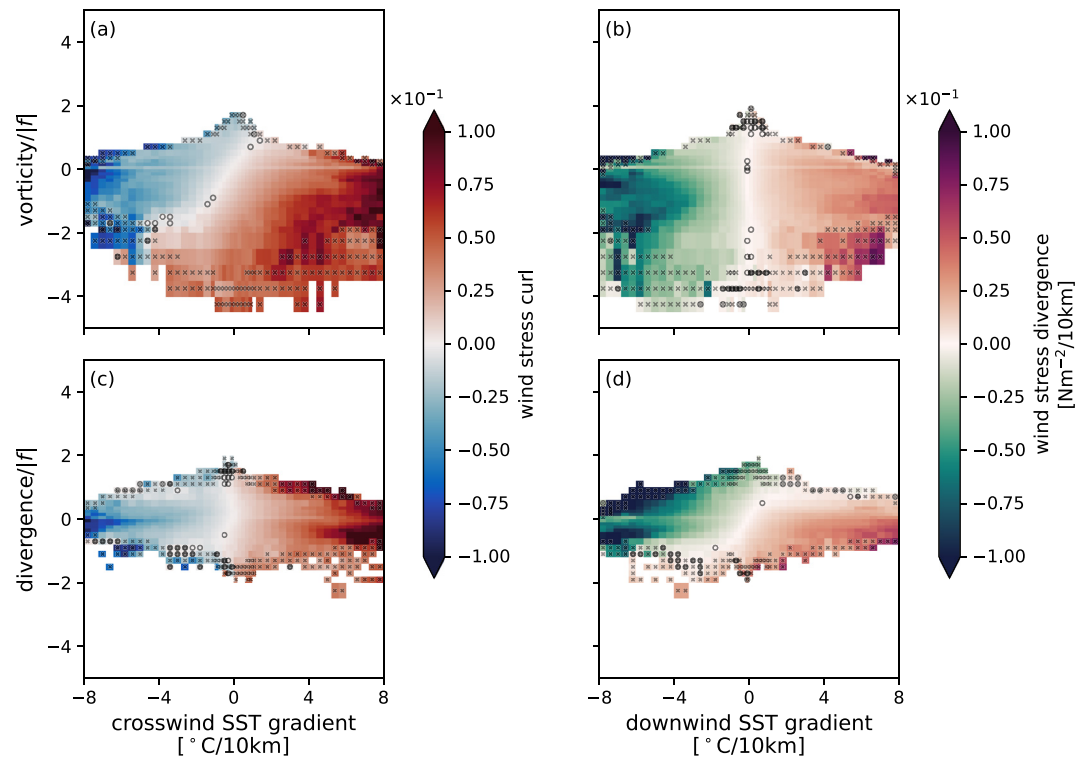


**Figure 2.** Conditional mean plots, conditioned on surface ocean vorticity or divergence and crosswind or downwind SST gradients, colored by mean values of either wind stress curl or wind stress divergence. Cross marks indicate bins with less than 50 points after removing data outside of mean  $\pm 1$  standard deviation. Circles indicate bins with standard error that is larger than the mean value. (a) The joint influence of vorticity and crosswind SST gradient on wind stress curl. (b) TFB from downwind SST gradient on wind stress divergence. (c) TFB from crosswind SST gradient on wind stress curl. (d) The joint influence of ocean divergence and downwind SST gradient on wind stress divergence. The slope of the zero-line (white in all panels) indicates the level of interaction and competition between surface vorticity/divergence and crosswind/downwind SST gradients in generating small-scale features in the wind stress fields. Evidence of sub-mesoscale dynamics is indicated by regions where the magnitude of  $Ro = \zeta/f$  is greater than 1 and is positively skewed (Figure 1).

vorticity, which causes wind stress curl to decrease with increasing vorticity, at fixed crosswind SST gradients. Together, this causes the zero-line (white) in wind stress curl to be tilted between the independent TFB- and CFB-dominant regimes. CFB constructively reinforces TFB feedback in the second (negative SST gradient and positive vorticity) and fourth (positive SST gradient and negative vorticity) quadrants, while destructively attenuating or even reversing the sign of the wind stress curl anomaly in the first (positive SST gradient and vorticity) and third (negative SST gradient and vorticity) quadrants. The combined influence is also present in Figure 2d, in which wind stress divergence is a function of both ocean surface divergence and downwind SST gradient. The constructive interaction between both feedbacks suggests that anomalously large wind stress curl or divergence occurs at large magnitudes of SST gradients and surface vorticity or divergence values, when they have the opposite signs. In Figure 2a, the jointly-generated wind stress curl approaches anomalously positive values that are over  $0.1 \text{ N m}^{-2}/10 \text{ km}$ , about 20 times stronger than in previous mesoscale studies (e.g., Chelton et al., 2004). This enhancement at small scales is also consistent with Strobach et al. (2022)'s 1D study on sub-mesoscale thermal feedback. These results also confirm, in a realistic numerical setting, that strong sub-mesoscale surface ocean divergence imprints on wind stress divergence, first shown in an idealized simulation by Chen et al. (2022). Although high-resolution 1D studies show enhanced feedback impact, they neglect variations from the other feedback and tend to underestimate wind stress curl or divergence, which is illustrated in Section 3.2.

### 3.2. Vorticity and Crosswind SST Gradient: Contribution and Variability

Based on the interaction between both feedbacks, in this section we test the hypothesis that most variance in wind stress fields can be explained by a combination of ocean surface vorticity/divergence and cross/downwind SST

gradients when the wind stress field is not dominated by synoptic events. The following analysis is focused on the dependence of wind stress curl on surface vorticity and crosswind SST gradients, but the same approach applies to wind stress divergence (see SI). We propose a dependent, bivariate, as opposed to univariate, and linear model to reconstruct wind stress curl:

$$\nabla \times \tau = \alpha \zeta / |f| + \beta \nabla_c \text{SST}. \quad (1)$$

$\nabla_c \text{SST}$  stands for crosswind SST gradients. The coefficients  $\alpha$  and  $\beta$  are solved for simultaneously by inverting the matrix whose columns correspond to vorticity scaled by  $|f|$  and crosswind SST gradients scaled by 10 km within the subdomain and over the desired time scales. The coefficients vary with the chosen normalization, but the relative contributions of the two terms on the right-hand side of Equation 1 are not dependent on normalizations. These coefficients are directly related to the 2D wind stress curl distributions, such that the ratio of  $\alpha$  and  $\beta$  corresponds to the zero-line slope (not shown) in Figure 2a. To assess the importance of the combined TFB and CFB, we compare the 2D dependent reconstruction to wind reconstructions due to CFB and TFB alone, as well as the linear sum of these two cases, for example, with  $\alpha$  and  $\beta$  coefficients determined independently.

Among the various reconstruction approaches, the ones that incorporate both feedbacks (2D and 1D current + thermal) provide a more accurate representation of the variance of wind stress curl (Figure 3). We solve for the 2D and 1D coefficients at hourly intervals in the energetic subdomain (Figure 1) and reconstruct the wind stress curl linearly based on Equation 1. Notably, the reconstructed wind stress curl has similar magnitudes using the bivariate 2D and 1D current + thermal approaches (Figures 3b, 3e and 3g, 3j). By comparison, univariate reconstruction performances are based on only one feedback, 1D current (Figures 3c and 3h) or 1D thermal (Figures 3d and 3i), fluctuate in time, suggesting that CFB or TFB dominance can vary even in a localized region. To statistically quantify their agreement with the simulated wind stress curl, the hourly Pearson correlation coefficient squared  $r^2$  is shown in Figure 3k for each method. Agreement between the two time series of  $r^2$  reconstructed by both feedback suggests similar spatial structures, while 1D current or 1D thermal feedback preferably recovers vorticity or filamentary structures, respectively. The  $r^2$  values indicate that skill in reconstructing wind stress curl improves when both feedbacks are involved. Specifically, the 1D current and 1D thermal reconstructions have 40% and 10% larger domain-averaged root-mean-square error (RMSE) for the three-month period (Figure 3l) as compared to the 2D reconstruction. The 1D independent sum slightly under-performs the 2D approach, with 3% more RMSE. However, caution should be taken in interpreting the reconstruction performance, as Equation 1 is limited when large-scale wind stress curl anomalies pass through the subdomain, potentially linked to synoptic events, as discussed in Section 4.

The 2D coefficients improve the wind stress curl reconstruction, but their values are time dependent (Figure 4).  $\alpha$  and  $\beta$  are calculated as in Equation 1 with one-, five-, and fifteen-day time windows within the energetic domain. For each case, the coefficients are calculated by updating the center of the window by one day; the values are plotted at the window midpoint in Figures 4b and 4c. Wintertime daily-calculated  $\alpha$  has a mean of  $-0.017 \pm 0.006 \text{ N m}^{-2}/10 \text{ km}$  and  $\beta$  has  $0.013 \pm 0.007 \text{ N m}^{-2}/^\circ\text{C}$ . The standard deviation for both coefficients reduces to  $\sim 0.003$  at 15-day time scale. The ratio,  $\beta/|\alpha|$ , across all three windowing time scales is about 0.8  $10 \text{ km}/^\circ\text{C}$ , which is consistent with the zero-line slope in Figure 2a.

We explored a wide range of physical properties at the air-sea interface that could contribute to variations in  $\alpha$  and  $\beta$ , and find that the most relevant are wind speed and air-sea temperature difference, respectively (Figures 4a and 4d). Within one-, five-, and fifteen-day time windows, wind speed at 10 m and each coefficient are scattered and the correlation between them is quantified with Pearson linear coefficients  $r_{W_\alpha}$  and  $r_{W_\beta}$  (Figures 4e and 4f). Absolute values of  $r_{W_\alpha}$  and  $r_{W_\beta}$  both increase with windowing length. Having  $r_{W_\alpha} > 0.8$  indicates that  $\alpha$  has a tight linear correlation with wind speed; this is weaker between  $\beta$  and wind speed with  $r_{W_\beta}$  ranging from 0.6 to 0.8. Indeed, when 1D binned means and standard deviations of  $\alpha$  and  $\beta$  are calculated as a function of wind speed (with bin sizes  $1 \text{ m s}^{-1}$ ),  $\beta$  has a spread that is twice as large compared with  $\alpha$ , on average (Figures 4e and 4f). We explore  $\beta$ 's relationship with air-sea temperature difference, noting that the quadratic drag coefficient of wind stress calculation,  $C_d$ , depends on this temperature difference. The correlation,  $r_{T_\beta}$  (Figure 4g), ranges from 0.4 to 0.7, with the largest  $r_{T_\beta}$  occurring for one-day time windows. The implications of the correlation dependence on time scale are discussed in Section 4.

#### 4. Discussion

This study emphasizes the importance of a 2D perspective on wind-front interactions at sub-mesoscales that accounts for the joint impact of TFB and CFB. This is illustrated by the distribution of wind stress curl as a

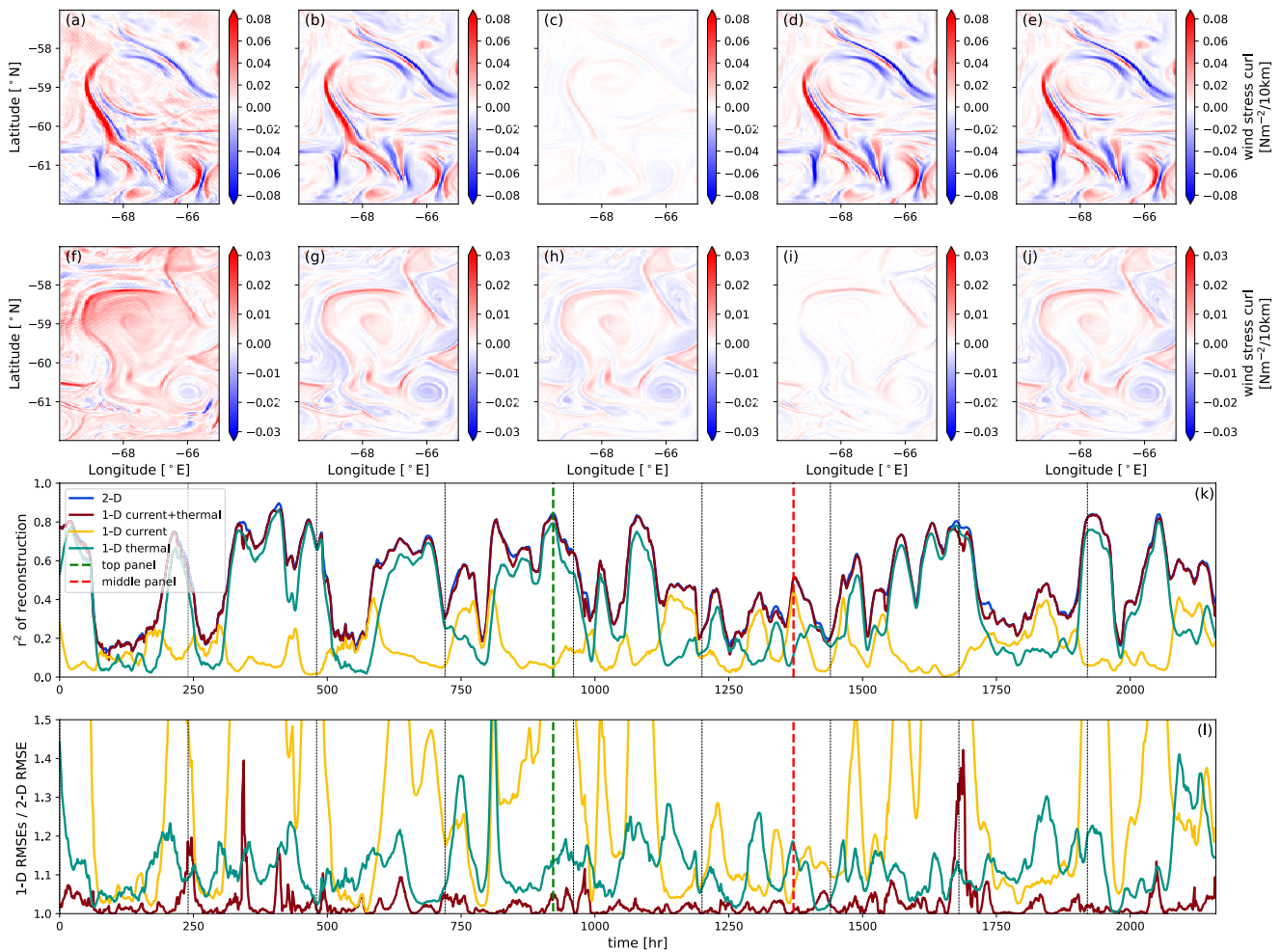


**Figure 3.** Illustration of reconstruction performances with simulated wind stress curl snapshots and hourly reconstruction variability. The top two panels (a–j), from left to right, show: (a, f) wind stress curl from the numerical simulation, (b, g) wind stress curl estimated by 2D dependent coefficients for both current and thermal feedback, (c, h) reconstruction based on 1D current feedback, (d, i) reconstruction based on 1D thermal feedback, (e, j) reconstruction from the linear sum of the 1D current and thermal feedbacks. Pearson linear correlation coefficients squared ( $r^2$ ) of each reconstruction and simulated wind stress curl are calculated per hour in (k). The root-mean square error of all 1-D reconstruction methods as well as the 2-D error are averaged through the subdomain in (l). The 1D current RMSE ratio curve is cropped, but reaches a maximum value of 2.98. The dashed lines indicate an instance of thermal and current feedback dominance that correspond to panels (a–e) and (f–j), respectively. Black dashed lines are 10 days separations.

function of surface vorticity and crosswind SST gradient (Figure 2). Incorporation of both feedbacks improves the skill of hourly wind stress field estimations compared with the traditional (univariate 1D) approaches (Figure 3). These relationships are summarized in terms of coefficients  $\alpha$  and  $\beta$  that describe the dependence on vorticity and crosswind SST gradients, respectively. The coefficient fluctuations are strongly correlated with variations in domain-averaged wind speed and air-sea temperature difference, respectively. In this section, we discuss implications of these small-scale wind-front interactions (Figure 2) as well as some limitations of the linear reconstruction.

Both TFB and CFB are required to accurately reconstruct wind stress field variability (Figure 3). Wind stress curl reconstructions are similar using either a 2D dependent sum or 1D current + thermal sum. Yet, using TFB or CFB alone leads to a larger domain-averaged RMSE, up to 60% and 190%, respectively. This occurs because the dominant feedback can vary with time (Figures 3k and 3l).

However, when both feedbacks are taken into account, the 2D dependent sum does not significantly outperform the 1D independent current + thermal sum. Thus, the interaction between TFB and CFB, at least in this simulation, remains largely linear from larger scales,  $O(100)$  km, to the resolved scales in this study,  $O(10)$  km, including regions where  $Ro \gtrsim 1$ . The accuracy of the 1D independent sum may deteriorate as the model resolution

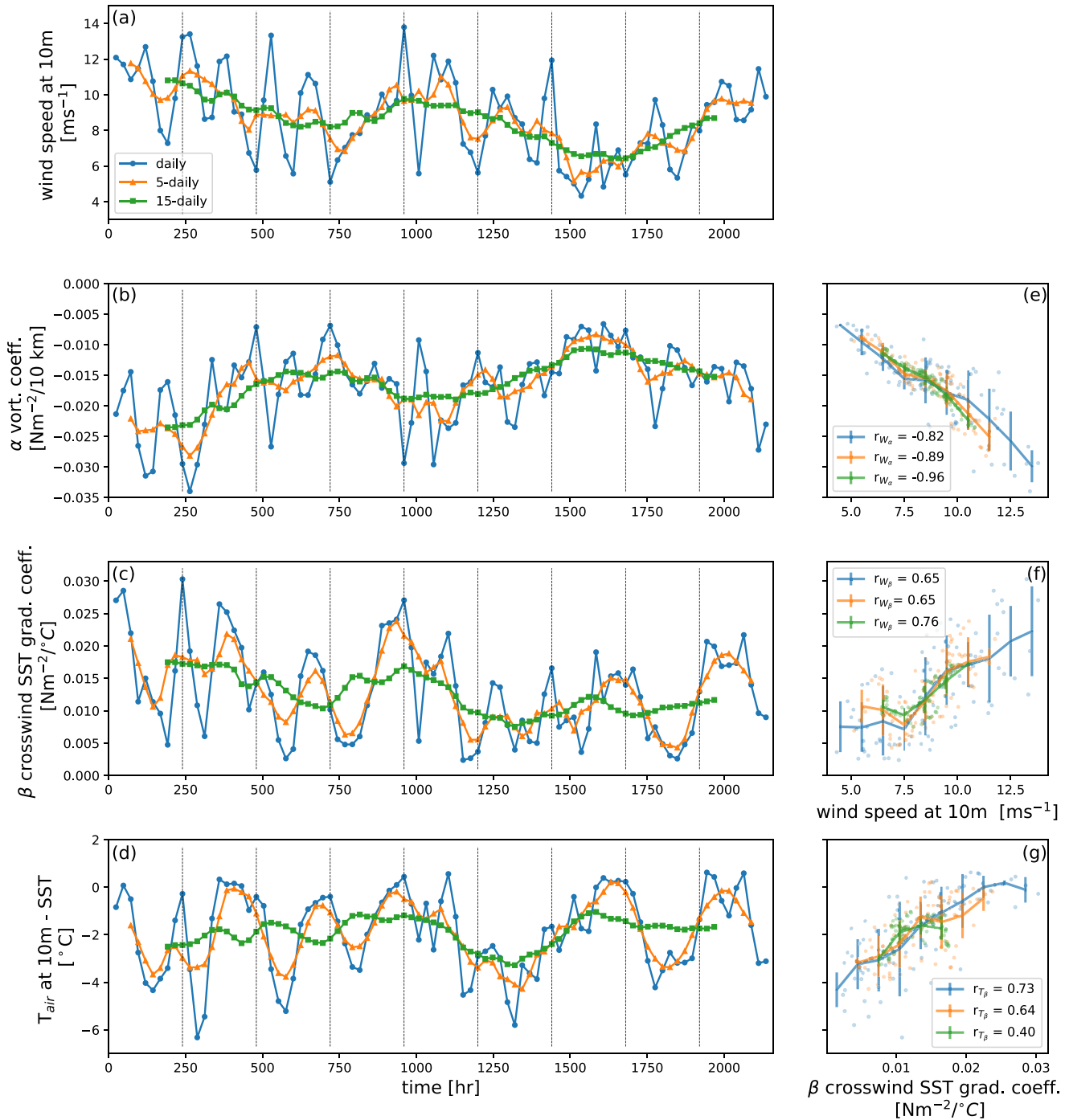


**Figure 4.** Variability of coefficients  $\alpha$  and  $\beta$  and their correlation with wind speed and air-sea temperature difference. Temporal evolution of (a) wind speed, (b)  $\alpha$ , (c)  $\beta$ , and (d) air-sea temperature difference (air temperature at 10 m – SST). The temporal variability is spatially averaged over the domain and over the same time period in which  $\alpha$  and  $\beta$  are obtained. (e) Correlation between wind speed and  $\alpha$  with Pearson correlation coefficient  $r_{W_\alpha}$ . (f) Correlation between wind speed and  $\beta$  with Pearson correlation coefficient  $r_{W_\beta}$ . (g) Correlation between air-sea temperature difference and  $\beta$  with Pearson correlation coefficient  $r_{T_\beta}$ .

increases, allowing for stronger and non-linear fronts. The temporal scale at which the upper ocean vorticity and SST fields evolve may also alter the relative importance of CFB and TFB.

While consideration of both vorticity and SST gradients improves wind stress curl reconstruction over 1D individual estimates, there remain periods when the inferred wind stress curl field differs significantly from the

simulated output, at least as measured by  $r^2$  (Figure 3). Further analysis of the reconstructed snapshots during these periods as well as the RMSE suggests a more nuanced relationship. During high  $r^2$  events ( $r^2 > 0.6$ ), the simulated wind stress curl is dominated by vorticity and strain structures that reflect those at the ocean surface. In most of the anomalously low  $r^2$  events ( $r^2 < 0.2$ ), the simulation is characterized by a large-scale, anomalous wind stress curl event that obscures the underlying fine-scale structures, which is potentially related to synoptic storms. The proposed 2D coefficients support reconstruction of the slowly-varying wind stress curl structures, therefore leading to occasional low  $r^2$  values when synoptic transient events dominate the wind field. Indeed, removing the domain averaged wind stress derivatives at those instances recovers some fine-scale structures and raises  $r^2$  by 25%–50%.

Spatially, the CFB and TFB coefficients are not uniform throughout the domain, but are instead tied to coherent structures, such as filamentary strain or eddy vorticity centers (Balwada et al., 2021) as diagnosed by the Okubo-Weiss parameter (SI). This information may be useful for future observational campaigns, similar to the Sub-Mesoscale Ocean Dynamics Experiment (S-MODE) (Farrar et al., 2020), in terms of experiment design and real-time adaptive sampling. The different characteristic time scales of variability for  $\alpha$  and  $\beta$  as well as the differing correlations between the two coefficients and various physical properties suggest that CFB and TFB vary in response to different physical processes. Vorticity coefficients  $\alpha$  are linearly correlated with wind stress magnitude ( $r_{W\alpha} > 0.8$ ) for all three time windows (Figure 4e), indicating an almost instantaneous domain-wide adjustment to wind stress curl through changes in relative velocities. The TFB coefficient  $\beta$  correlates with both air-sea temperature difference and wind speed, yet the spread is almost twice as large in the wind speed correlation. Since the highest  $r_{T\beta}$  occurs at daily time scales (Figure 4g), we infer that air-sea temperature differences and the daily atmospheric heating/cooling cycle explain most of the variance for high frequency variations of  $\beta$ . This is consistent with Desbiolles et al. (2023), which identified a correlation at a daily time scale between 1D thermal feedback and air-sea temperature gradients in reanalysis data. In contrast,  $r_{W\beta}$  remains moderate for all time scales. The larger spread may be explained by a longer time for wind speed adjustment through downward momentum mixing in the atmospheric boundary layer as compared to air-sea temperature thermal adjustments. A more detailed mechanistic analysis of  $\beta$  and its relationship to wind speed and air-sea temperature gradient is needed. The relative contributions from each feedback are expected to vary both temporally and spatially throughout the global ocean; mapping this behavior is left for future studies.

This study has focused on simulated, wintertime properties from Drake Passage, Southern Ocean. This region hosts especially vigorous mesoscale and sub-mesoscale flow fields (Luecke et al., 2017), enabling strong wind-front interactions and the potential for enhanced ventilation. Compared to the rest of the global ocean, properties unique to the Southern Ocean include stronger surface winds (Flexas et al., 2019) (Figure 1b), sharper surface density gradients, deeper mixed layers (Dong et al., 2008), and weaker stratification, which, combined with the connectedness to the world ocean basins (Talley, 2013), make the Southern Ocean a critical location where the impact of wind-front interactions and modifications to air-sea fluxes may have a global impact (Nicholson et al., 2022). The stronger sub-mesoscale modification to wind stress curl in this study could potentially enhance vertical velocities in the upper ocean through Ekman dynamics (Gaube et al., 2015; Seo et al., 2016). The impact of wind-front interactions on the transport of tracers, ventilation, and upper ocean stratification in the Southern Ocean are key directions for future study (Morrison et al., 2022; Swart et al., 2023).

## 5. Conclusion

Estimation of both the structure and magnitude of wind stress curl or divergence improves when the combined impact of surface ocean velocity and SST gradients, or the synergy of current and thermal feedbacks, are considered. Conditional mean plots of wind stress curl and wind stress divergence illustrate that in the Southern Ocean, the two feedbacks constructively and destructively interact and jointly control anomalies in the wind fields at sub-mesoscale. Temporal variability of each feedback is tied to physical properties such as wind speed or air-sea temperature difference, or both, implying the underlying mechanical and thermodynamical mechanisms of wind-front interactions. The results presented in this study are based on an energetic domain that is relevant to other strong western boundary currents. Yet, the mechanism of wind-front interactions is generic and applies to other ocean regions with varied intensity. A more comprehensive quantification of the two feedbacks is indispensable to constrain the calculation of air-sea fluxes and ocean surface properties. This study highlights the need for future observational endeavors with collocated measurements of surface currents, SST, and surface wind stress.

## Data Availability Statement

The coupled ocean-atmosphere simulation used in this study is accessible through: (a) any NASA Ames Super-computer at ~dmenemen/c1440\_llc2160/; (b) xmitgcm: <https://xmitgcm.readthedocs.io>; (c) NASA Ames data portal: <https://data.nas.nasa.gov/ecco/>. Example calculation and plotting codes are here: <https://doi.org/10.5281/zenodo.8231130>.

## Acknowledgments

YB acknowledges support from the National Aeronautics and Space Administration (NASA) Science Mission Directorate FINESST program under Award No. 80NSSC21K1635. AFT and ABVB were supported by NASA Grant 80NSSC19K1004; ABVB received additional support from the NSF award OCE-2241822 and NASA Grant 80NSSC23K0979. PK acknowledges support from the SWOT Science Team, and the QuikSCAT mission. HT and DM carried research at the Jet Propulsion Laboratory, California Institute of Technology, under a contract with NASA, with grants from the Physical Oceanography and Modeling, Analysis, and Prediction programs. High-End computing was provided by the NASA Advanced Supercomputing Division at the Ames Research Center.

## References

- Balwada, D., Smith, K. S., & Abernathy, R. (2018). Submesoscale vertical velocities enhance tracer subduction in an idealized Antarctic circumpolar current. *Geophysical Research Letters*, *45*(18), 9790–9802. <https://doi.org/10.1029/2018gl079244>
- Balwada, D., Xiao, Q., Smith, S., Abernathy, R., & Gray, A. R. (2021). Vertical fluxes conditioned on vorticity and strain reveal submesoscale ventilation. *Journal of Physical Oceanography*, *51*(9), 2883–2901. <https://doi.org/10.1175/jpo-d-21-0016.1>
- Barkan, R., Molemaker, M. J., Srinivasan, K., McWilliams, J. C., & D'Asaro, E. A. (2019). The role of horizontal divergence in submesoscale frontogenesis. *Journal of Physical Oceanography*, *49*(6), 1593–1618. <https://doi.org/10.1175/jpo-d-18-0162.1>
- Buckingham, C. E., Naveira Garabato, A. C., Thompson, A. F., Brannigan, L., Lazar, A., Marshall, D. P., et al. (2016). Seasonality of submesoscale flows in the ocean surface boundary layer. *Geophysical Research Letters*, *43*(5), 2118–2126. <https://doi.org/10.1002/2016gl068009>
- Bye, J. A. (1985). Large-scale momentum exchange in the coupled atmosphere-ocean. In *Elsevier oceanography series* (Vol. 40, pp. 51–61). Elsevier. [https://doi.org/10.1016/S0422-9894\(08\)70702-5](https://doi.org/10.1016/S0422-9894(08)70702-5)
- Callies, J., Barkan, R., & Naveira Garabato, A. (2020). Time scales of submesoscale flow inferred from a mooring array. *Journal of Physical Oceanography*, *50*(4), 1065–1086. <https://doi.org/10.1175/jpo-d-19-0254.1>
- Chang, P., Zhang, S., Danabasoglu, G., Yeager, S. G., Fu, H., Wang, H., et al. (2020). An unprecedented set of high-resolution earth system simulations for understanding multiscale interactions in climate variability and change. *Journal of Advances in Modeling Earth Systems*, *12*(12), e2020MS002298. <https://doi.org/10.1029/2020ms002298>
- Chelton, D. B., Esbensen, S. K., Schlax, M. G., Thum, N., Freilich, M. H., Wentz, F. J., et al. (2001). Observations of coupling between surface wind stress and sea surface temperature in the eastern tropical pacific. *Journal of Climate*, *14*(7), 1479–1498. [https://doi.org/10.1175/1520-0442\(2001\)014<1479:ooocsw>2.0.co;2](https://doi.org/10.1175/1520-0442(2001)014<1479:ooocsw>2.0.co;2)
- Chelton, D. B., Schlax, M. G., Freilich, M. H., & Milliff, R. F. (2004). Satellite measurements reveal persistent small-scale features in ocean winds. *Science*, *303*(5660), 978–983. <https://doi.org/10.1126/science.1091901>
- Chelton, D. B., Schlax, M. G., & Samelson, R. M. (2007). Summertime coupling between sea surface temperature and wind stress in the California current system. *Journal of Physical Oceanography*, *37*(3), 495–517. <https://doi.org/10.1175/jpo3025.1>
- Chelton, D. B., Schlax, M. G., & Samelson, R. M. (2011). Global observations of nonlinear mesoscale eddies. *Progress in Oceanography*, *91*(2), 167–216. <https://doi.org/10.1016/j.pocean.2011.01.002>
- Chelton, D. B., & Xie, S.-P. (2010). Coupled ocean-atmosphere interaction at oceanic mesoscales. *Oceanography*, *23*(4), 52–69. <https://doi.org/10.5670/oceanog.2010.05>
- Chen, X., Dewar, W., Chassignet, E., Bourassa, M., Morey, S., & Gopalakrishnan, G. (2022). On the feedback between air-sea turbulent momentum flux and oceanic submesoscale processes. *Journal of Geophysical Research: Oceans*, *127*(10), e2022JC018767. <https://doi.org/10.1029/2022jc018767>
- Desbiolles, F., Meroni, A. N., Renault, L., & Pasquero, C. (2023). Environmental control of wind response to sea surface temperature patterns in reanalysis dataset. *Journal of Climate*, *36*(12), 1–31. <https://doi.org/10.1175/jcli-d-22-0373.1>
- Dong, S., Sprintall, J., Gille, S. T., & Talley, L. (2008). Southern ocean mixed-layer depth from Argo float profiles. *Journal of Geophysical Research*, *113*(C6), C06013. <https://doi.org/10.1029/2006jc004051>
- Dove, L. A., Balwada, D., Thompson, A. F., & Gray, A. R. (2022). Enhanced ventilation in energetic regions of the Antarctic circumpolar current. *Geophysical Research Letters*, *49*(13), e2021GL097574. <https://doi.org/10.1029/2021gl097574>
- Dove, L. A., Thompson, A. F., Balwada, D., & Gray, A. R. (2021). Observational evidence of ventilation hotspots in the southern ocean. *Journal of Geophysical Research: Oceans*, *126*(7), e2021JC017178. <https://doi.org/10.1029/2021jc017178>
- Dove, L. A., Vigliano, G. A., Thompson, A. F., Flexas, M. M., Cason, T. R., & Sprintall, J. (2023). Controls on wintertime ventilation in southern Drake Passage. *Geophysical Research Letters*, *50*(5), e2022GL102550. <https://doi.org/10.1029/2022gl102550>
- Farrar, J. T., D'Asaro, E., Rodriguez, E., Shcherbina, A., Czech, E., Matthias, P., et al. (2020). S-mode: The sub-mesoscale ocean dynamics experiment. In *IGARSS 2020-2020 IEEE international geoscience and remote sensing symposium* (pp. 3533–3536). <http://doi.org/10.1109/IGARSS39084.2020.9323112>
- Flexas, M. M., Thompson, A. F., Torres, H. S., Klein, P., Farrar, J. T., Zhang, H., & Menemenlis, D. (2019). Global estimates of the energy transfer from the wind to the ocean, with emphasis on near-inertial oscillations. *Journal of Geophysical Research: Oceans*, *124*(8), 5723–5746. <https://doi.org/10.1029/2018jc014453>
- Foussard, A., Lapeyre, G., & Plougonven, R. (2019). Storm track response to oceanic eddies in idealized atmospheric simulations. *Journal of Climate*, *32*(2), 445–463. <https://doi.org/10.1175/jcli-d-18-0415.1>
- Frenger, I., Gruber, N., Knutti, R., & Münnich, M. (2013). Imprint of southern ocean eddies on winds, clouds and rainfall. *Nature Geoscience*, *6*(8), 608–612. <https://doi.org/10.1038/ngeo1863>
- Gaube, P., Chelton, D. B., Samelson, R. M., Schlax, M. G., & O'Neill, L. W. (2015). Satellite observations of mesoscale eddy-induced Ekman pumping. *Journal of Physical Oceanography*, *45*(1), 104–132. <https://doi.org/10.1175/jpo-d-14-0032.1>
- Gruber, N., Landschützer, P., & Lovenduski, N. S. (2019). The variable southern ocean carbon sink. *Annual Review of Marine Science*, *11*(1), 159–186. <https://doi.org/10.1146/annurev-marine-121916-063407>
- Hoskins, B. J., & Bretherton, F. P. (1972). Atmospheric frontogenesis models: Mathematical formulation and solution. *Journal of the Atmospheric Sciences*, *29*, 295.
- Luecke, C., Arbic, B., Bassette, S., Richman, J., Shriver, J., Alford, M., et al. (2017). The global mesoscale eddy available potential energy field in models and observations. *Journal of Geophysical Research: Oceans*, *122*(11), 9126–9143. <https://doi.org/10.1002/2017jc013136>
- Marshall, J., & Speer, K. (2012). Closure of the meridional overturning circulation through southern ocean upwelling. *Nature Geoscience*, *5*(3), 171–180. <https://doi.org/10.1038/ngeo1391>
- McWilliams, J. C. (2016). Submesoscale currents in the ocean. *Proceedings of the Royal Society A: Mathematical, Physical and Engineering Sciences*, *472*(2189), 20160117. <https://doi.org/10.1098/rspa.2016.0117>

- Morrison, A. K., Waugh, D. W., Hogg, A. M., Jones, D. C., & Abernathy, R. P. (2022). Ventilation of the southern ocean pycnocline. *Annual Review of Marine Science*, 14(1), 405–430. <https://doi.org/10.1146/annurev-marine-010419-011012>
- Nicholson, S. A., Whitt, D. B., Fer, I., du Plessis, M. D., Lebéhot, A. D., Swart, S., et al. (2022). Storms drive outgassing of CO<sub>2</sub> in the subpolar southern ocean. *Nature Communications*, 13(1), 158. <https://doi.org/10.1038/s41467-021-27780-w>
- O'Neill, L. W., Chelton, D. B., & Esbensen, S. K. (2012). Covariability of surface wind and stress responses to sea surface temperature fronts. *Journal of Climate*, 25(17), 5916–5942. <https://doi.org/10.1175/jcli-d-11-00230.1>
- Rai, S., Hecht, M., Maltrud, M., & Aluie, H. (2021). Scale of oceanic eddy killing by wind from global satellite observations. *Science Advances*, 7(28), eabf4920. <https://doi.org/10.1126/sciadv.abf4920>
- Renault, L., Masson, S., Oerder, V., Colas, F., & McWilliams, J. C. (2023). Modulation of the oceanic mesoscale activity by the mesoscale thermal feedback to the atmosphere. *Journal of Physical Oceanography*, 53(7), 1651–1667. <https://doi.org/10.1175/jpo-d-22-0256.1>
- Renault, L., Masson, S., Oerder, V., Jullien, S., & Colas, F. (2019). Disentangling the mesoscale ocean-atmosphere interactions. *Journal of Geophysical Research: Oceans*, 124(3), 2164–2178. <https://doi.org/10.1029/2018jc014628>
- Renault, L., McWilliams, J. C., & Gula, J. (2018). Dampening of submesoscale currents by air-sea stress coupling in the Californian upwelling system. *Scientific Reports*, 8(1), 1–8. <https://doi.org/10.1038/s41598-018-31602-3>
- Renault, L., McWilliams, J. C., & Masson, S. (2017). Satellite observations of imprint of oceanic current on wind stress by air-sea coupling. *Scientific Reports*, 7(1), 1–7. <https://doi.org/10.1038/s41598-017-17939-1>
- Renault, L., Molemaker, M. J., McWilliams, J. C., Shchepetkin, A. F., Lemarié, F., Chelton, D., et al. (2016). Modulation of wind work by oceanic current interaction with the atmosphere. *Journal of Physical Oceanography*, 46(6), 1685–1704. <https://doi.org/10.1175/jpo-d-15-0232.1>
- Rooth, C., & Xie, L. (1992). Air-sea boundary layer dynamics in the presence of mesoscale surface currents. *Journal of Geophysical Research*, 97(C9), 14431–14438. <https://doi.org/10.1029/92jc01296>
- Seo, H., Miller, A. J., & Norris, J. R. (2016). Eddy–wind interaction in the California current system: Dynamics and impacts. *Journal of Physical Oceanography*, 46(2), 439–459. <https://doi.org/10.1175/jpo-d-15-0086.1>
- Seo, H., O'Neill, L. W., Bourassa, M. A., Czaja, A., Drushka, K., Edson, J. B., et al. (2023). Ocean mesoscale and frontal-scale ocean–atmosphere interactions and influence on large-scale climate: A review. *Journal of Climate*, 36(7), 1981–2013. <https://doi.org/10.1175/jcli-d-21-0982.1>
- Siegelman, L., Klein, P., Rivière, P., Thompson, A. F., Torres, H. S., Flexas, M. M., & Menemenlis, D. (2020). Enhanced upward heat transport at deep submesoscale ocean fronts. *Nature Geoscience*, 13(1), 50–55. <https://doi.org/10.1038/s41561-019-0489-1>
- Small, R. J., Bryan, F. O., Bishop, S. P., & Tomas, R. A. (2019). Air–sea turbulent heat fluxes in climate models and observational analyses: What drives their variability? *Journal of Climate*, 32(8), 2397–2421. <https://doi.org/10.1175/jcli-d-18-0576.1>
- Small, R. J., de Zoete, S. P., Xie, S., O'Neill, L., Seo, H., Song, Q., et al. (2008). Air–sea interaction over ocean fronts and eddies. *Dynamics of Atmospheres and Oceans*, 45(3–4), 274–319. <https://doi.org/10.1016/j.dynatmoce.2008.01.001>
- Strobach, E., Klein, P., Molod, A., Fahad, A. A., Trayanov, A., Menemenlis, D., & Torres, H. (2022). Local air-sea interactions at ocean mesoscale and submesoscale in a western boundary current. *Geophysical Research Letters*, 49(7), e2021GL097003. <https://doi.org/10.1029/2021gl097003>
- Swart, S., du Plessis, M. D., Nicholson, S. A., Monteiro, P. M. S., Dove, L. A., Thomalla, S., et al. (2023). The Southern Ocean mixed layer and its boundary fluxes: Fine-scale observational progress and future research priorities. *Philosophical Transactions of the Royal Society A*, 381(2249). <https://doi.org/10.1098/rsta.2022.0058>
- Takatama, K., & Schneider, N. (2017). The role of back pressure in the atmospheric response to surface stress induced by the Kuroshio. *Journal of the Atmospheric Sciences*, 74(2), 597–615. <https://doi.org/10.1175/jas-d-16-0149.1>
- Talley, L. D. (2013). Closure of the global overturning circulation through the Indian, Pacific, and southern oceans: Schematics and transports. *Oceanography*, 26(1), 80–97. <https://doi.org/10.5670/oceanog.2013.07>
- Taylor, J. R., & Thompson, A. F. (2023). Submesoscale dynamics in the upper ocean. *Annual Review of Fluid Mechanics*, 55(1), 103–127. <https://doi.org/10.1146/annurev-fluid-031422-095147>
- Thomas, L. N., Tandon, A., & Mahadevan, A. (2008). Submesoscale processes and dynamics. Ocean modeling in an eddying regime. *Geophysical Monograph Series*, 177, 17–38.
- Torres, H. S., Klein, P., Wang, J., Wineteer, A., Qiu, B., Thompson, A. F., et al. (2022). Wind work at the air-sea interface: A modeling study in anticipation of future space missions. *Geoscientific Model Development*, 15(21), 8041–8058. <https://doi.org/10.5194/gmd-15-8041-2022>
- Xu, Y., & Scott, R. B. (2008). Subtleties in forcing eddy resolving ocean models with satellite wind data. *Ocean Modelling*, 20(3), 240–251. <https://doi.org/10.1016/j.ocemod.2007.09.003>